

Article

Petrogenesis of the Early Cretaceous Tiantangshan A-Type Granite, Cathaysia Block, SE China: Implication for the Tin Mineralization

Ru-Ya Jia ^{1,2}, Guo-Chang Wang ^{3,*}, Lin Geng ⁴, Zhen-Shan Pang ^{1,2}, Hong-Xiang Jia ⁵,
Zhi-Hui Zhang ^{1,2}, Hui Chen ^{1,2} and Zheng Liu ⁶

- ¹ Development and Research Center, China Geological Survey, Beijing 100037, China; cgsjruya@163.com (R.-Y.J.); pzs927@163.com (Z.-S.P.); zzh1102114@126.com (Z.-H.Z.); chenhui_nju@163.com (H.C.)
- ² Technical Guidance Center for Mineral Resources Exploration, Ministry of Natural Resources of the People's Republic of China, Beijing 100120, China
- ³ Yunnan Key Laboratory for Palaeobiology, Yunnan University, Kunming 650091, China
- ⁴ China Geological Survey, Beijing 100037, China; genglin66@126.com
- ⁵ School of Earth Sciences and Resources, China University of Geosciences, Beijing 100083, China; cugbjiahongxiang@126.com
- ⁶ School of Resource Environment and Earth Science, Yunnan University, Kunming 650091, China; liuzheng.0311@163.com
- * Correspondence: gcwang@ynu.edu.cn

Received: 14 March 2019; Accepted: 24 April 2019; Published: 29 April 2019



Abstract: The newly discovered Tiantangshan tin polymetallic deposit is located in the southeast Nanling Range, Cathaysia block, Southeast China. The tin orebodies are mainly hosted in the greisen and the fractured alteration zones of the tufflava and trachydacite. However, the genetic relationship between the hidden alkali-feldspar granite and volcanic rocks and the tin mineralization remains poorly understood. This paper presents SHRIMP zircon U–Pb dating, whole-rock major and trace element analyses, as well as Nd isotopic data of the trachydacite and alkali-feldspar granite. The SHRIMP zircon U–Pb dating of the alkali-feldspar granite and trachydacite yields weight mean $^{206}\text{Pb}/^{238}\text{U}$ ages of 138.4 ± 1.2 , and 136.2 ± 1.2 Ma, respectively. These granitic rocks have high levels of SiO_2 (64.2–75.4 wt%, mostly > 68 wt%), alkalis ($\text{K}_2\text{O} + \text{Na}_2\text{O} > 8.3$ wt%), REE (except for Eu), HFSE ($\text{Zr} + \text{Nb} + \text{Ce} + \text{Y} > 350$ ppm) and Ga/Al ratios ($10,000 \times \text{Ga/Al} > 2.6$), suggesting that they belong to the A-type granite. According to the high Y/Nb and Yb/Ta ratios, they can be further classified into A₁ subtype. Their $\varepsilon_{\text{Nd}}(\text{T})$ range from –3.8 to –6.5. They were likely generated by the assimilation-fractional crystallization (AFC) of the coeval oceanic island basalts -like basaltic magma. This study suggests that the A₁ type granite is also a potential candidate for the exploration of tin deposits.

Keywords: A-type granite; tin mineralization; Tiantangshan tin polymetallic deposit; SE China

1. Introduction

The enrichment mechanism of Sn in tin deposits is of great importance for studies on its mineralization and may provide useful guidance for tin prospecting. Previous studies have revealed that most primary tin deposits are closely related to granitic rocks in time and space [1], indicating a possible genetic relationship. The fractional crystallization of granitic rocks plays a vital role in the origin of the tin deposit [2], whereas the geochemical heritage of granitic rocks has been shown to exert a relatively limited influence on tin mineralization [3]. The in situ fractional crystallization of

tin granitic rocks is characterized by significant depletion of Ba and Sr, a drop in the TiO_2/Ta ratio [4], and an increase in the level of Rb [2]. As result, the resultant tin granitic rocks display a distinct geochemical specialization in Sn and other incompatible elements (e.g., F, Li, B, Cs) [1]. The extreme differentiation of these tin granitic rocks suggests that they might represent the most evolved phase of mantle-derived magmas [3]. Recent studies showed that many major tin deposit-related granitic rocks can be classified as A-type granite [5–7], which are geochemically characterized by high levels of K_2O , high incompatible trace element contents (including REE, Zr, Nb and Ta), elevated $\text{Fe}/(\text{Fe} + \text{Mg})$ and $\text{K}_2\text{O}/\text{Na}_2\text{O}$, as well as low concentrations of trace elements compatible in mafic silicate and feldspar [8,9]. A-type granite can be further divided into two subtypes, A_1 and A_2 , based on their geochemical differences [10]. The A_1 -type granite has been postulated to be generated by the assimilation-fractional crystallization (AFC) of oceanic-island basalt, whereas its A_2 -type counterpart is thought to be derived by the partial melting of continental crustal sources [9]. Based on the results of previous investigations, the A_1 -type granite may present the highly differentiated mantle-derived magma [9]. However, its genetic relationship with tin mineralization remains poorly understood.

The Nanling Range, located in the middle area of the South China, is well known for its abundant tin-polymetallic ore deposits. This region is characterized by widespread and intensive late Mesozoic magmatism, as well as the associated mineralization. The tin deposits are spatially, temporally and metallogenically associated with the coeval granites [11]. Most tin granites in the Nanling Range are metaluminous to weakly peraluminous biotite (hornblende) granite with an A-type granite affinity [7,12]. They are enriched in Nb, Zr, Ce, Y and HFSEs with relatively high alkali contents [7,12]. Most can be further classified as A_2 type granite [13,14]. They have been interpreted as derived from the partial melting of Precambrian crustal rocks [15]. However, A_1 -type tin granite in the Nanling Range is rarely reported in previous studies.

The Tiantangshan tin polymetallic deposit, located in the southeast of the Nanling Range (Figure 1), has a tin reserve of 25 kt with an average grade of 0.5% and a WO_3 reserve of 7 kt with an average grade of 0.3%. $^{40}\text{Ar}/^{39}\text{Ar}$ dating of the biotite that coexists with the cassiterite in the ore samples yielded an isochron age of 133.5 ± 0.75 Ma [16]. The orebodies are mainly hosted in the greisen and the fractured alteration zones of tufflava and trachydacite (Figure 2). Further geological examination by drilling revealed a hidden alkali-feldspar granite underneath the greisen (Figure 3). Nevertheless, the genetic relationship between tin mineralization and the intrusive-volcanic rocks remains enigmatic. In this contribution, we present detailed SHRIMP zircon U–Pb dating, whole-rock major and trace element analyses, as well as Nd isotope data of trachydacite and alkali-feldspar granite in Tiantangshan deposit to explore their genetic relationships. Our experiment results led us to tentatively conclude that the alkali-feldspar granite and trachydacite can both be categorized as A_1 -type generated from the AFC of the coeval OIB-like basaltic magma. Furthermore, the current study suggests that A_1 -type Tiantangshan alkali-feldspar granite is genetically associated with tin mineralization.

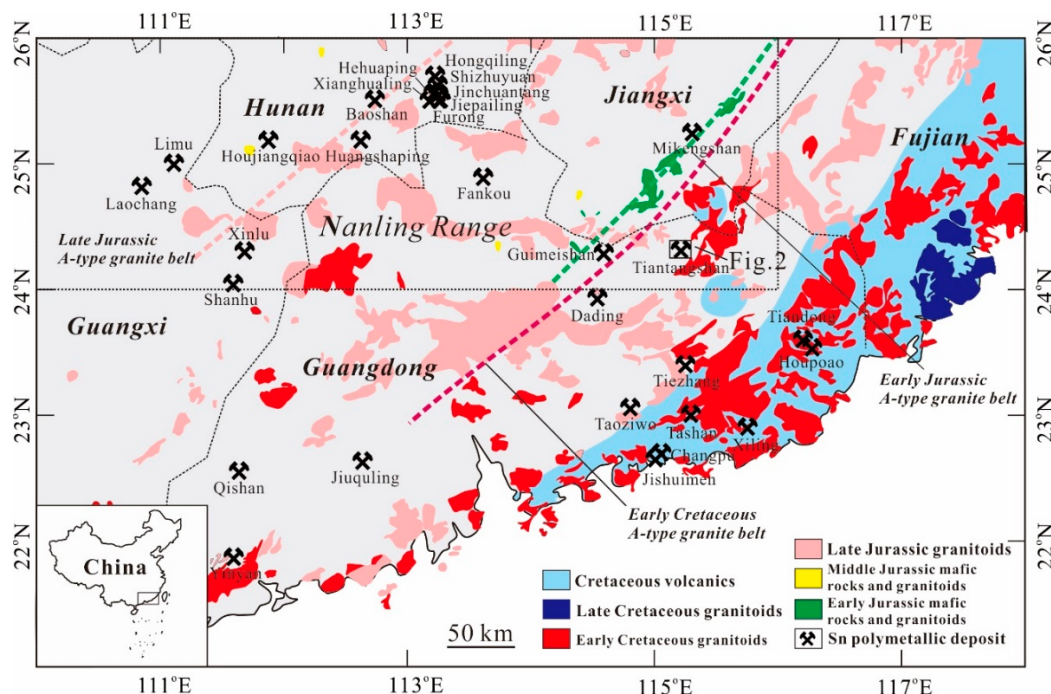


Figure 1. A sketch map of tin polymetallic deposits in the Nanling Range and neighboring area. Also shown are the late Mesozoic volcanic-intrusive complex and the A-type granite belts, modified after [15].

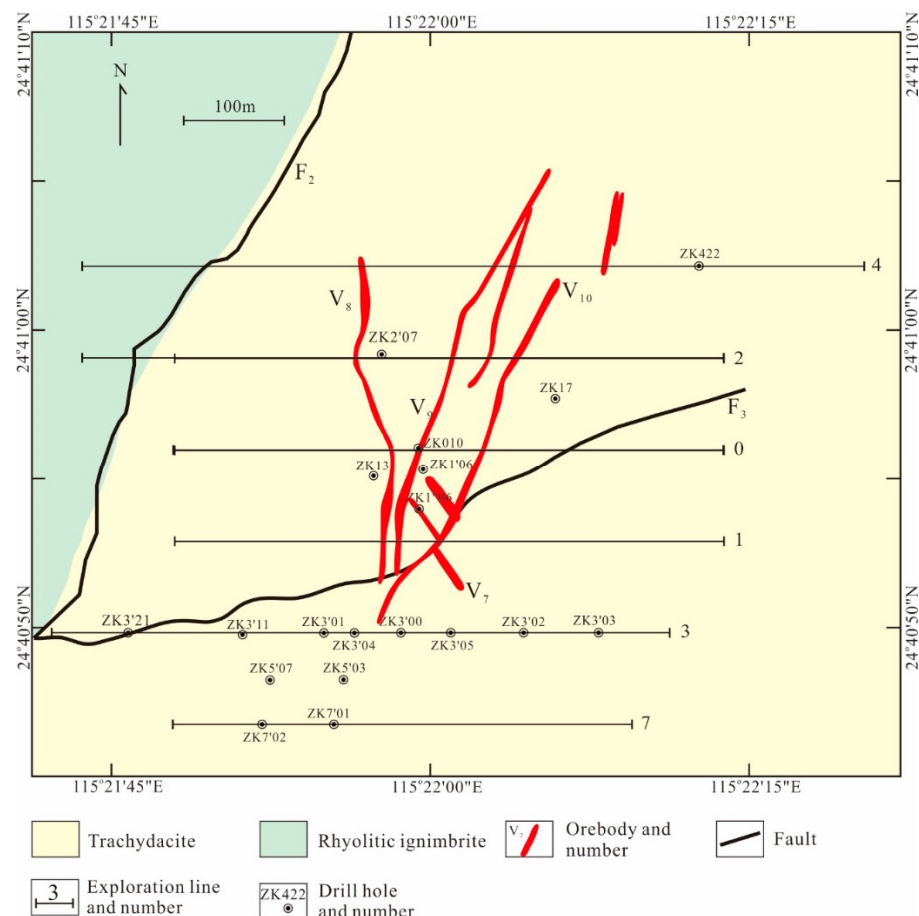


Figure 2. Geological schematic map of the Tiantangshan tin polymetallic deposit.

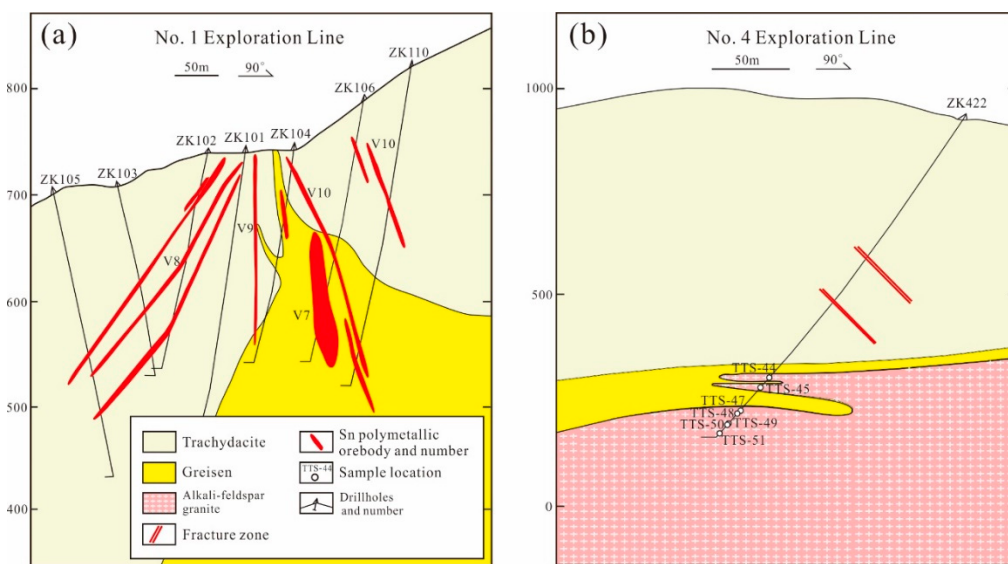


Figure 3. Geological cross-section along the exploration line No.1 (a) and No.4 (b).

2. Tectonic Settings

2.1. Regional Geology

The South China Block is composed of the Yangtze Block in the north and the Cathaysia Block in the south. The Cathaysia Block consists of Paleoproterozoic to Early Neoproterozoic metamorphic rocks, Late Neoproterozoic to Paleozoic continental to neritic marine sediments, and Mesozoic terrestrial clastics. The South China Block experienced multiple tectono-magmatic events during the Mesozoic, including its collision with the Indochina Block at ca. 240–230 Ma [17,18], its collage with the North China block along the Dabie–Sulu orogenic belt at ca. 220–245 Ma [19], and the westward subduction of the Palaeo-Pacific Plate that likely started in the Late Triassic [15]. These events triggered the intensive and extensive Mesozoic magmatism as well as the related tin mineralization in SE China [20]. Triassic granitoids are mainly exposed over the inland regions of the South China, whereas their Jurassic to Cretaceous equivalents are distributed in the form of 600 km wide volcanic-intrusive complex belt, parallel to the present coastline. Studies have indicated that these granitoids mostly belong to the (high-K) calc-alkaline series, and can be genetically classified as I- and S-types [20,21]. In addition, Mesozoic A-type granite formed over different periods have also been identified. The Late Triassic (229–221 Ma) A-type granite occur as an ENE-trending belt, and are coincident with the Late Triassic mafic magmatism. On the other hand, the Early Jurassic (192–188 Ma), Late Jurassic (163–153 Ma), Early Cretaceous (141–124 Ma) and Late Cretaceous (101–91 Ma) A-type granite belts are all NNE-trending in parallel to the present coastline [15]. All these five belts were produced by repeated slab-advance-retreat of the Palaeo-Pacific plate [15].

The Nanling Range, a major E–W trending W–Sn metallogenic province, is situated within the northwestern margin of the Cathaysia Block (Figure 1), and includes most of the border areas of Hunan, Jiangxi, Fujian, Guangdong and Guangxi Provinces. The region is characterized by the late Mesozoic intensive multistage magmatism and large-scale mineralization of tin, tungsten, and other rare-metals. The tin polymetallic deposits mainly comprise of skarn and wolframite-bearing quartz veins with minor greisen types [11,22]. It has been suggested that the formation of these tin-bearing deposits can be divided into three distinct stages, including the Late Triassic (230–210 Ma), Mid–Late Jurassic (170–150 Ma) and Early–Mid Cretaceous (120–80 Ma) [22]. The Early Cretaceous tin polymetallic deposits in the Nanling Range are mainly located in the volcanic basins of Southeast Jiangxi and have not been vigorously investigated in previous studies possibly due to their comparatively smaller scale. The Tiantangshan tin polymetallic deposit is located in the southeast region of the Nanling Range, but

the petrogenesis of the hidden alkali-feldspar granite and trachydacite needs further study, and their possible genetic relationship with the tin deposit remains enigmatic.

2.2. Geology and Sampling of the Tiantangshan Tin Polymetallic Deposit

The newly explored Tiantangshan tin polymetallic deposit is located in the Mabugang town of Northeastern Guangdong (Figure 1). The stratigraphic sequence in the Tiantangshan deposit consists of the Late Jurassic Gaojiping Formation. The Gaojiping Formation is dominated by intermediate felsic lava and pyroclastic rocks, and can be further divided into three members from bottom to top that differ in their eruption cycles and the type of rocks that they contain [16]. The first member is more than 340 m thick and is exposed in the northwest of the mining area (Figure 2), consisting mainly of rhyolitic ignimbrite with minor breccia-bearing ignimbrite. The second member is about 280 to 350 m thick and hosts the tin orebodies (Figure 2), with a mineral composition of trachydacite, rhyolitic tuff, tuffaceous lava and crystal lithic tuff. The third member, over 550 m thick, mainly comprises rhyolitic breccia-bearing lava and rhyolitic lithic crystal tuff. Drilling reveals the concealed alkali-feldspar granite underneath the volcanic rocks (Figure 3b). The main structures in the mining area include NE-striking (F_3) and NNE-striking (F_2) faults. Three types of W-Sn orebodies can be identified in the Tiantangshan deposit, including greisen-, quartz vein- and fracture zones veined type. Typical hydrothermal alterations in the area encompass albitization, silicification, topazization, greisenization, biotitization, chloritization, sericitization, and fluoritization [16]. According to field and microscopic observations, the formation of the tin ores can be divided into four stages that can be distinguished by mineral assemblage: (1) Greisenization stage (stage I), (2) Quartz–cassiterite–wolframite stage (stage II), (3) Quartz–fluorite–cassiterite–sulfides stage (stage III) and (4) Post-ore stage (stage IV) [16].

In this study, the alkali-feldspar granite and trachydacite samples were collected from the core which drilled from the ZK422, ZK010 and –711 m underground tunnels. The alkali-feldspar granite consists of K-feldspar, plagioclase, quartz and biotite with a medium-grained granitic texture (Figure 4a,b). Greisen is made up of quartz, muscovite, topaz, chlorite, cassiterite, and rare pyrite (Figure 4c,d). On the other hand, the trachydacite mainly contains phenocrysts and matrix which consists of alkali-feldspar, plagioclase and quartz (Figure 4e,f).



Figure 4. (a,c,e) Photographs and (b,d,f) Photomicrographs (under crossed polar) of intrusive-volcanic rocks in Tiantangshan tin polymetallic deposits: (a) and (b) are alkali-feldspar granite; (c) and (d) are greisen; and (e) and (f) are trachydacite. Kfs, K-feldspar; Q, quartz; Bt, biotite; Toz, topaz; Mus, muscovite; Pl, plagioclase; Max, matrix.

3. Analytical Methods

3.1. SHRIMP Zircon U–Pb Dating

Zircon in situ U–Th–Pb isotope analyses were conducted using a SHRIMP-II at the Beijing SHRIMP Center, Chinese Academy of Geological Sciences, Beijing, China, following the similar analytical procedure described by [23]. A primary 20–30 $\mu\text{m}\cdot\text{O}^{2-}$ ion beam with an intensity of 3–6 nA was used to bombard the zircon surfaces. The raster time was set to 120–200 s. Each analysis consisted of five scans. Reference zircons for elemental abundance calibration included 91,500 (U = 91 ppm), SL13 (U = 238 ppm), and M257 (U = 840 ppm) [23–25]. TEMORA with a $^{206}\text{Pb}/^{238}\text{U}$ age of 417.0 ± 1.8 Ma was used for calibration [26]. Data were processed by SQUID and Isoplot [27]. Common Pb corrections

were based on the measured ^{204}Pb contents. Uncertainties for individual analyses were quoted at 1σ , whereas the errors for the weighted mean ages were quoted at 2σ (95% confidence).

3.2. Major, Trace Elements and Nd Isotope of Intrusive-Volcanic Rocks

The alkali-feldspar granite and trachydacite samples were crushed and powdered to 200 meshes in an agate mortar. Whole-rock major and trace elements analyses of the alkali-feldspar granite samples were performed at the Key Laboratory of Orogenic Belts and Crustal Evolution, Ministry of Education, School of Earth and Space Sciences, Peking University. Major elements were analyzed with an X-ray fluorescence spectrometer on fused glass beads. The analytical uncertainty of oxide over 10 wt% is <1% while that of oxides below 10 wt% is <10%. Detailed methods for trace elements analyses were presented in [28]. Trace elements were characterized on a PerkinElmer Elan9000/DRCII/DRC-e ICP-MS. In brief, exactly 50 mg of sample powder were dissolved at 190 °C in a closed high-pressure Savillex Teflon beakers containing a mixture of 1 mL HF + 1 mL HNO₃ for 36 h. The resultant solution was then evaporated to dryness, followed by the addition of 1.5 mL of HNO₃, 1.5 mL of HF and 0.5 mL HClO₄. The beaker was subsequently capped and placed in an oven to allow the digestion to proceed at 180 °C for at least 48 h. Once the powders were completely digested, the residue was diluted in 50 mL of 1% HNO₃ for further analysis. The international reference samples GSR-1 (granite), GSR-2 (andesite) and GSR-9 (granodiorite) were used as controls. All of trace elements measurement showed an error below 5%.

Whole rock major and trace elements analyses of the trachydacite samples were conducted at the Analytical Laboratory of Beijing Research Institute of Uranium Geology, China National Nuclear Corporation. Whole rock major elements were analyzed by were analyzed on a Philips (Philips PW2404, Amsterdam, The Netherlands) X-ray fluorescence spectrometer (XRF). The test methods were based on GB/T 14506-2010 and had a precision that was better than 1% for the oxides over 10 wt% and 10% for the oxides below 10 wt%. Meanwhile, trace elements were analyzed by inductively coupled plasma mass spectrometry (ICP-MS) on an Agilent 7500a system using the same procedure described above, with a measurement uncertainty of 5%. Nd isotope analyses were performed at the Analytical Laboratory of Beijing Research Institute of Uranium Geology, China National Nuclear Corporation, following a previously established protocol [29,30]. Briefly, 100 mg of the sample powder was dissolved in a Teflon beaker containing a mixture of HF + HNO₃, followed by the separation and purification of Nd with conventional cation-exchange. The mass fractionation corrections of $^{143}\text{Nd}/^{144}\text{Nd}$ ratios were on the basis of $^{146}\text{Nd}/^{144}\text{Nd}$ of 0.7219. Total analytical blanks were 5×10^{-11} g for Sm-Nd.

4. Results

4.1. SHRIMP Zircon U-Pb Geochronology

SHRIMP zircon U-Pb dating results of two samples are summarized in Table 1 and illustrated in Figure 5. The zircons exhibit regular oscillatory magmatic zoning with a size distribution mostly between 100 and 200 μm and high Th/U ratios in the range of 0.4 to 0.98 (Table 1). Nine analyses of sample TTS-50 (alkali-feldspar granite) plot in a group on the Concordia curve and yield a weighted mean $^{206}\text{Pb}/^{238}\text{U}$ age of 138.4 ± 1.2 Ma (MSWD = 0.62) (Figure 5a). Eleven analyses for sample TTS-89 (trachydacite) plot in a group on the Concordia curve and yield a weighted mean $^{206}\text{Pb}/^{238}\text{U}$ age of 136.2 ± 1.2 Ma (MSWD = 0.49) (Figure 5b).

Table 1. SHRIMP zircon U–Pb dating for the Tiantangshan alkali-feldspar granite and trachydacite.

Spot	U (ppm)	Th (ppm)	Th/U	$^{206}\text{Pb}^*$ (ppm)	$^{207}\text{Pb}/^{206}\text{Pb}$	$\pm\%$	$^{207}\text{Pb}^*/^{235}\text{U}$	$\pm\%$	$^{206}\text{Pb}^*/^{238}\text{U}$	$\pm\%$	$^{206}\text{Pb}/^{238}\text{U}$ (Age/Ma)	$\pm 1\sigma$
Sample TTS-50 (alkali-feldspar granite)												
1.1	1179	513	0.45	22.1	0.0489	4.8	0.1453	5	0.02155	1.3	137.4	1.7
2.1	1859	976	0.54	35.5	0.0497	5.5	0.1487	5.6	0.02168	1.3	138.3	1.7
3.1	1034	399	0.4	19.6	0.0481	4.9	0.1442	5.1	0.02173	1.3	138.6	1.8
6.1	1241	1099	0.91	23.4	0.0488	3	0.1473	3.2	0.02188	1.3	139.5	1.7
7.1	1005	460	0.47	19.1	0.0496	3.4	0.151	3.7	0.02208	1.3	140.8	1.8
9.1	983	933	0.98	18.2	0.0492	3.5	0.1457	3.7	0.02145	1.3	136.8	1.7
12.1	1058	584	0.57	20.4	0.0485	8.4	0.146	8.5	0.0218	1.3	139	1.8
13.1	789	410	0.54	14.5	0.0482	3.4	0.1423	3.7	0.02139	1.3	136.4	1.8
15.1	1143	767	0.69	21.8	0.048	4.8	0.1443	4.9	0.02182	1.3	139.2	1.8
Sample TTS-89 (trachydacite)												
1.1	357	254	0.74	6.53	0.0489	6.5	0.1434	6.7	0.02125	1.4	135.5	1.9
2.1	401	312	0.8	7.48	0.0487	5	0.1453	5.2	0.02164	1.4	138	1.9
4.1	328	225	0.71	6.07	0.0502	7.8	0.148	7.9	0.02136	1.5	136.3	2.0
5.1	260	167	0.66	4.82	0.0478	6	0.1416	6.1	0.02147	1.5	136.9	2.0
6.1	361	228	0.65	6.58	0.0521	7	0.15	7.1	0.02091	1.5	133.4	1.9
7.1	248	208	0.87	4.62	0.0493	11	0.146	11	0.0214	1.6	136.5	2.1
8.1	226	176	0.8	4.16	0.0478	10	0.14	10	0.02123	1.6	135.4	2.1
9.1	224	167	0.77	4.14	0.0503	13	0.148	13	0.02132	1.7	136	2.3
10.1	487	311	0.66	8.98	0.0473	7.8	0.139	7.9	0.02125	1.4	135.5	1.9
11.1	147	117	0.82	2.7	0.0477	6.9	0.1401	7	0.02133	1.6	136	2.2
12.1	305	266	0.9	5.72	0.0477	4.4	0.1427	4.6	0.0217	1.4	138.4	1.9

All the spots are localized on the around the zircon rims, common lead corrected using ^{204}Pb , $^{206}\text{Pb}^*$ is radiogenic lead. The error estimate is 1σ .

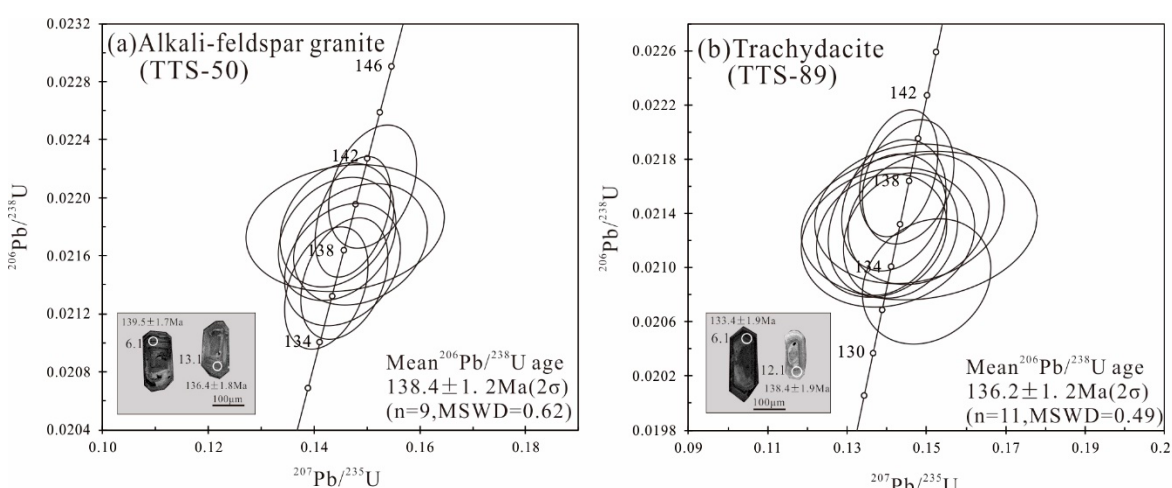


Figure 5. SHRIMP zircon U–Pb concordant curves for the Tiantangshan alkali-feldspar granite (a) and trachydacite (b).

4.2. Major, Trace Elements of Whole Rocks

The alkali-feldspar granite samples have SiO_2 contents of 73.0–75.4 wt% (Tables 2 and 3), and are characterized by relatively high heavy rare earth elements (HREEs), significant depletion of Eu, Ba and Sr, as well as notable negative Eu, Ba and Sr anomalies (Figure 6a,b). In comparison, the trachydacite contain lower abundances of SiO_2 that range from 68.5 to 70.0 wt.%, and are enriched in light rare earth elements (LREE) but depleted in HREEs with notable negative Eu anomalies (Figure 6c). Furthermore, the trachydacite samples are enriched in large ion lithophile elements (LILE) and depleted in high field strength elements (HFSE), while showing notable negative Ta–Nb and Ti anomalies (Figure 6d).

Table 2. Major (wt%), trace element (ppm), Nd isotope compositions and $T_{DM2}(Nd)$ ages of the Tiantangshan alkali-feldspar granite and trachydacite.

Sample	TTS-44		TTS-45		TTS-47		TTS-48		TTS-49		TTS-50	
Rock Type	Alkali-feldspar Granite											
	wt %	± wt %	wt %	± wt %	wt %	± wt %	wt %	± wt %	wt %	± wt %	wt %	± wt %
SiO ₂	75.2	0.8	73.0	0.7	73.7	0.7	75.4	0.8	74.8	0.7	75.2	0.8
TiO ₂	0.10	0.01	0.11	0.01	0.10	0.01	0.11	0.01	0.10	0.01	0.11	0.01
Al ₂ O ₃	12.7	0.1	13.7	0.1	13.2	0.1	12.8	0.1	12.8	0.1	12.9	0.1
FeO	1.11	0.11	2.2	0.2	1.65	0.17	1.65	0.17	1.31	0.13	1.37	0.14
Fe ₂ O ₃	1.58	0.16	2.36	0.24	1.99	0.20	1.72	0.17	1.53	0.15	1.58	0.16
FeO ^T	2.54	0.25	4.32	0.43	3.45	0.35	3.20	0.32	2.69	0.27	2.79	0.28
MnO	0.04	0.004	0.10	0.01	0.11	0.01	0.06	0.01	0.05	0.005	0.04	0.004
MgO	0.15	0.02	0.19	0.02	0.08	0.01	0.06	0.01	0.08	0.01	0.05	0.01
CaO	0.65	0.07	0.99	0.10	0.89	0.09	0.48	0.05	0.58	0.06	0.62	0.06
Na ₂ O	3.31	0.33	2.80	0.28	3.26	0.33	4.10	0.41	4.80	0.48	4.52	0.45
K ₂ O	5.13	0.51	5.49	0.55	5.55	0.56	4.58	0.46	4.59	0.46	4.23	0.42
P ₂ O ₅	0.02	0	0.02	0	0.01	0	0.02	0	0.02	0	0.02	0
LOI	0.93		1.12		0.90		0.56		0.67		0.54	
	ppm	± ppm	ppm	± ppm	ppm	± ppm	ppm	± ppm	ppm	± ppm	ppm	± ppm
Rb	754	38	851	43	749	37	670	34	806	40	616	31
Ba	68.1	3.4	61.2	3.1	75.6	3.8	50.1	2.5	63.9	3.2	54.3	2.7
Th	59.0	3.0	65.5	3.3	64.8	3.2	64.2	3.2	74.5	3.7	64.3	3.2
U	18.9	0.9	16.9	0.8	19.9	1.0	12.0	0.6	18.9	0.9	18.7	0.9
Nb	117	6	143	7	122	6	136	7	132	7	123	6
Ta	20.3	1.0	23.9	1.2	18.1	0.9	18.8	0.9	16.9	0.8	17.3	0.9
Zr	177	9	204	10	203	10	212	11	169	8	199	10
Hf	10.6	0.5	12.3	0.6	12.5	0.6	12.8	0.6	12.3	0.6	11.3	0.6
Sr	16.5	0.8	26.8	1.3	20.5	1.0	16.1	0.8	20.1	1.0	21.2	1.1
Y	73.0	3.7	77.6	3.9	78.1	3.9	74.4	3.7	77.6	3.9	84.0	4.2
Pb	26.1	1.3	14.2	0.7	51.5	2.6	22.4	1.1	39.3	2.0	26.7	1.3
La	55.7	2.8	56.9	2.8	59.7	3.0	60.1	3.0	55.1	2.8	59.4	3.0
Ce	109	5	111	6	116	6	113	6	109	5	113	6
Pr	12.9	0.6	13.0	0.7	13.4	0.7	13.3	0.7	12.9	0.6	13.7	0.7
Nd	44.8	2.2	40.3	2.0	45.1	2.3	46.7	2.3	45.0	2.3	49.1	2.5
Sm	8.99	0.45	8.27	0.4	9.18	0.46	9.55	0.48	8.87	0.44	10.2	0.5
Eu	0.20	0.01	0.22	0.01	0.23	0.01	0.18	0.01	0.26	0.01	0.21	0.01
Gd	8.20	0.41	8.27	0.41	8.59	0.43	8.59	0.43	8.35	0.42	9.07	0.45
Tb	1.86	0.09	1.84	0.09	1.95	0.10	1.95	0.10	1.99	0.10	2.10	0.11
Dy	11.8	0.6	11.9	0.6	11.7	0.6	11.4	0.6	12.7	0.6	13.1	0.7
Ho	2.50	0.13	2.65	0.13	2.60	0.13	2.57	0.13	2.77	0.14	2.80	0.14
Er	7.10	0.36	7.73	0.39	7.68	0.38	7.25	0.36	8.37	0.42	8.17	0.41
Tm	1.41	0.07	1.55	0.08	1.54	0.08	1.48	0.07	1.77	0.09	1.54	0.08
Yb	8.66	0.43	9.85	0.49	9.81	0.49	9.29	0.46	11.3	0.6	10.2	0.5
Lu	1.13	0.06	1.31	0.07	1.32	0.07	1.27	0.06	1.50	0.1	1.37	0.07
Ga	28.9	1.4	32.1	1.6	31.3	1.6	32.1	1.6	31.7	1.6	31.7	1.6
W	6.22	0.31	8.71	0.44	5.76	0.29	4.83	0.24	3.00	0.15	4.41	0.22
Sn	18.3	0.9	27.8	1.4	31.5	1.6	19.2	1.0	21.3	1.1	17.1	0.9
Cu	2.77	0.14	2.40	0.12	2.87	0.14	2.05	0.10	2.06	0.10	1.84	0.09
Zn	325	16	537	27	250	13	52.4	2.6	87.7	4.4	50.3	2.5
Mo	0.81	0.04	0.97	0.05	0.63	0.03	0.44	0.02	0.43	0.02	0.54	0.03
REE	274		281		290		289		280		292	
LREE	231		236		245		245		231		244	
HREE	42.7		45.1		45.2		43.8		48.8		48.4	
LREE/HREE	5.42		5.24		5.41		5.59		4.74		5.04	
(La/Yb) _N	4.61		4.14		4.37		4.64		3.50		4.18	
δEu	0.07		0.07		0.08		0.06		0.09		0.07	
¹⁴⁷ Sm/ ¹⁴⁴ Nd	0.1212		0.1240		0.1230		0.1236				0.1255	
¹⁴³ Nd/ ¹⁴⁴ Nd	0.512352		0.512379		0.512275		0.512354				0.512374	
±2σ	0.000006		0.000006		0.000012		0.000007				0.000009	
ε _{Nd(T)}	-4.2		-3.8		-5.8		-4.2				-3.9	
T _{DM2} (Nd)(Ma)	1277		1238		1402		1277				1249	

± wt %, ± ppm: analytical uncertainty.

Table 3. Major (wt%), trace element (ppm), Nd isotope compositions and $T_{DM2}(Nd)$ ages of the Tiantangshan alkali-feldspar granite and trachydacite.

Sample	TTS-51		TTS-56		TTS-60		TTS-41		TTS-89	
Rock Type	Alkali-feldspar Granite					Trachydacite				
	wt %	± wt %	wt %	± wt %	wt %	± wt %	wt %	± wt %	wt %	± wt %
SiO ₂	75.3	0.8	69.9	0.7	64.2	0.6	70.0	0.7	68.5	0.7
TiO ₂	0.10	0.01	0.27	0.03	0.64	0.06	0.32	0.03	0.26	0.03
Al ₂ O ₃	12.8	0.1	14.7	0.1	15.1	0.2	15.0	0.1	14.7	1.5
FeO	1.37	0.14	1.65	0.17	2.83	0.28	1.14	0.11	1.98	0.20
Fe ₂ O ₃	1.47	0.15	1.62	0.16	2.74	0.27	1.17	0.12	1.76	0.18
FeOT	2.69	0.27	3.46	0.35	5.90	0.59	2.44	0.24	3.97	0.40
MnO	0.04	0.004	0.16	0.02	0.12	0.01	0.03	0.003	0.08	0.01
MgO	0.04	0.004	0.38	0.04	0.42	0.04	0.31	0.03	0.22	0.02
CaO	0.63	0.06	0.45	0.04	1.55	0.15	0.65	0.07	1.31	0.13
Na ₂ O	4.16	0.42	3.42	0.34	5.03	0.50	3.50	0.35	2.36	0.24
K ₂ O	4.72	0.47	6.32	0.63	4.94	0.49	6.74	0.67	6.57	0.66
P ₂ O ₅	0.01	0	0.04	0	0.07	0.01	0.06	0.01	0.05	0
LOI	0.61		0.74		1.38		0.74		1.37	
	ppm	± ppm	ppm	± ppm	ppm	± ppm	ppm	± ppm	ppm	± ppm
Rb	709	35	757	38	1222	61	863	43	819	41
Ba	49.8	2.5	548	27	396	20	329	16	257	13
Th	68.3	3.4	37.2	1.9	44.1	2.2	34.4	1.7	36.5	1.8
U	21.5	1.1	6.10	0.31	5.90	0.30	6.80	0.34	6.30	0.32
Nb	116	6	52.1	2.6	49.3	2.5	45.3	2.3	43.4	2.2
Ta	16.6	0.8	3.70	0.19	2.50	0.13	2.70	0.14	2.40	0.12
Zr	163	8	248	12	224	11	184	9	155	8
Hf	8.8	0.4	7.60	0.38	6.90	0.35	5.70	0.29	5.30	0.27
Sr	18.6	0.9	120	6	106	5	74.9	3.7	97.2	4.9
Y	83.8	4.2	50.4	2.5	49.0	2.4	27.4	1.4	41.1	2.1
Pb	37.5	1.9	40.8	2.0	149	7	21.6	1.1	23.1	1.2
La	59.8	3.0	83.2	4.2	91.4	4.6	92.3	4.6	97.5	4.9
Ce	115	6	169	8	181	9	186	9	209	10
Pr	13.8	0.7	17.6	0.9	19.4	1.0	19.8	1.0	22.0	1.10
Nd	44.7	2.2	63.0	3.2	68.8	3.4	68.6	3.4	76.4	3.8
Sm	9.41	0.47	10.1	0.5	12.1	0.6	12.0	0.6	12.4	0.6
Eu	0.20	0.01	1.07	0.05	0.91	0.05	0.63	0.03	0.70	0.04
Gd	8.89	0.44	8.70	0.44	9.28	0.46	8.38	0.42	9.37	0.47
Tb	2.10	0.11	1.36	0.07	1.38	0.07	1.06	0.05	1.29	0.06
Dy	12.5	0.6	7.99	0.40	7.85	0.39	4.85	0.24	6.84	0.34
Ho	2.76	0.14	1.62	0.08	1.56	0.08	0.84	0.04	1.30	0.07
Er	8.02	0.40	4.70	0.24	4.57	0.23	2.26	0.11	3.59	0.18
Tm	1.53	0.08	0.72	0.04	0.72	0.04	0.32	0.02	0.52	0.03
Yb	10.0	0.5	4.57	0.23	4.78	0.24	2.14	0.11	3.26	0.16
Lu	1.30	0.07	0.71	0.04	0.72	0.04	0.34	0.02	0.50	0.03
Ga	29.8	1.5	21.3	1.1	23.2	1.2	20.3	1.0	23.2	1.2
W	4.20	0.21	11.4	0.6	29.7	1.5	19.4	1.0	29.7	1.5
Sn	21.0	1.0	6.59	0.33	24.9	1.2	9.11	0.46	45.1	2.3
Cu	2.77	0.14	3.21	0.16	35.1	1.8	4.02	0.20	199	10
Zn	55.6	2.8	46.7	2.3	390	20	35.2	1.8	315	16
Mo	0.26	0.01	3.59	0.18	13.0	0.7	12.2	0.6	3.03	0.15
REE	293		375		405		400		434	
LREE	246		344		374		380		408	
HREE	47.1		30.4		30.9		20.2		26.7	
LREE/HREE	5.23		11.3		12.1		18.8		15.3	
(La/Yb) _N	4.30		13.1		13.7		31.0		21.5	
δEu	0.07		0.34		0.25		0.18		0.21	
¹⁴⁷ Sm/ ¹⁴⁴ Nd	0.1272								0.0981	
¹⁴³ Nd/ ¹⁴⁴ Nd	0.51236								0.512216	
±2σ	0.00009								0.000007	
ε _{Nd} (T)	-4.7								-6.5	
T _{DM2} (Nd)(Ma)	1311								1460	

± wt %, ± ppm: analytical uncertainty.

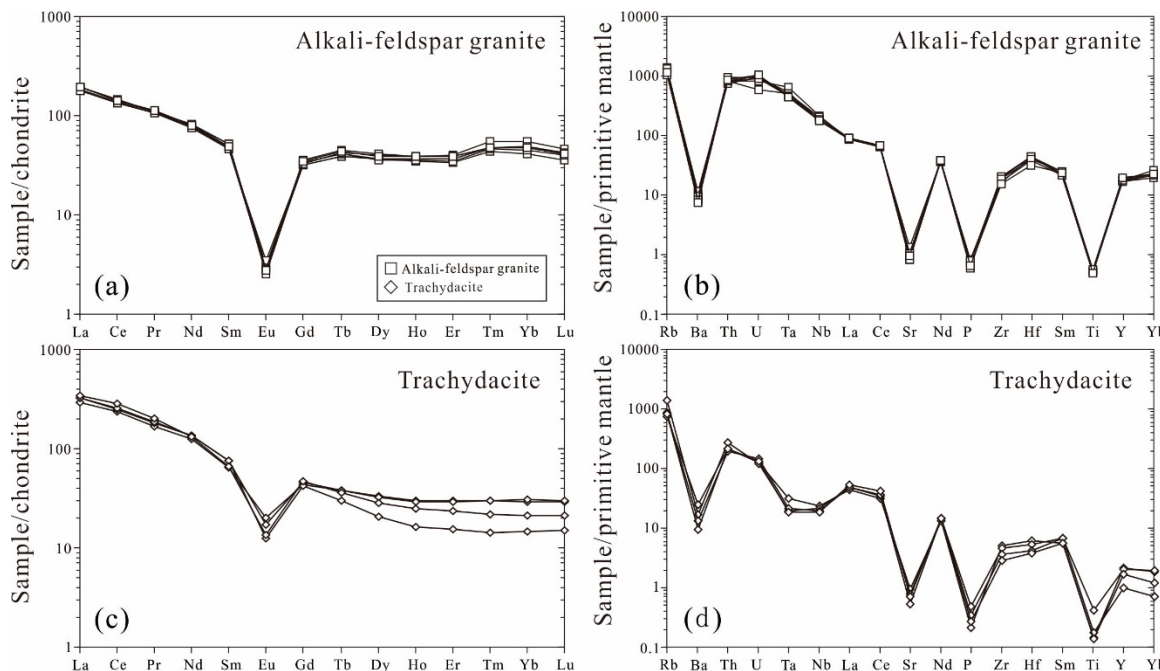


Figure 6. (a,c) Chondrite-normalized [31] REE patterns and (b,d) primitive mantle-normalized [32] trace element patterns for the Tiantangshan alkali-feldspar granite and trachydacite.

4.3. Nd Isotopes of Whole Rocks

The alkali-feldspar granites exhibit relatively narrow Nd isotopic compositions with $\varepsilon_{\text{Nd}}(\text{T})$ ranging from -3.8 to -5.8 (Figure 7), whereas the average $\varepsilon_{\text{Nd}}(\text{T})$ of trachydacite is comparatively lower at -6.5 . All the granitic rocks yield Mesoproterozoic T_{DM2} ages between 1.06 and 1.40 Ga.

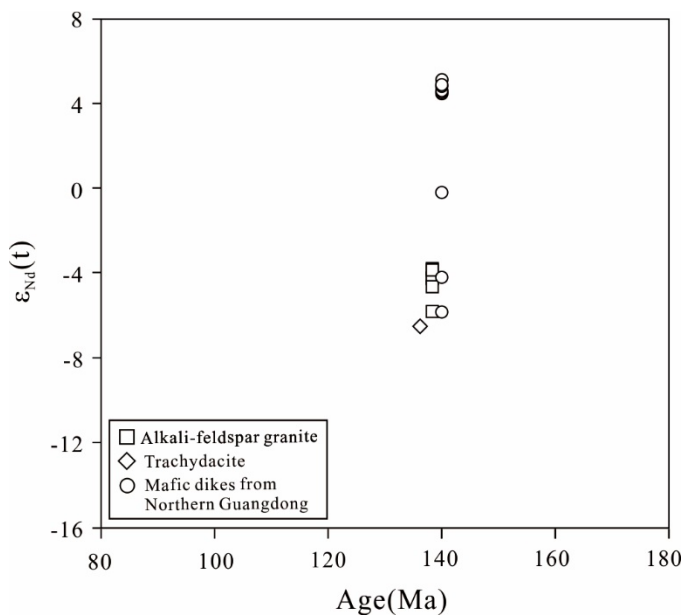


Figure 7. Age vs. $\varepsilon_{\text{Nd}}(\text{T})$ diagrams for the Tiantangshan alkali-feldspar granite and trachydacite. Also shown are the fields of the Early Cretaceous gabbros in northern Guangdong [33].

5. Discussion

5.1. Duration of the Magmatism and Hydrothermal Activities

Unlike zircon U–Pb age, biotite $^{40}\text{Ar}/^{39}\text{Ar}$ ages tend to reflect the cooling history of the minerals rather than their crystallization. In addition, they generally do not record early magmatic and hydrothermal events at $>350\text{ }^{\circ}\text{C}$. The time intervals between zircon U–Pb ages and biotite $^{40}\text{Ar}/^{39}\text{Ar}$ ages could indicate a prolonged magmatic-hydrothermal process and cooling history. Previous $^{40}\text{Ar}/^{39}\text{Ar}$ dating of biotite coexisting with cassiterite in the Tiantangshan deposit yielded an isochron age of $133.5 \pm 0.75\text{ Ma}$ [16]. In our present study, the $^{206}\text{Pb}/^{238}\text{U}$ ages of the alkali-feldspar granite and trachydacite in the same deposit are measured to be 138.4 ± 1.2 and $136.2 \pm 1.2\text{ Ma}$, respectively. Evidently, these felsic rocks have slightly older emplacement ages when compared to the biotite $^{40}\text{Ar}/^{39}\text{Ar}$ data. An alternative interpretation is that the relatively low closure temperature of the biotite rendered it sensitive and vulnerable to thermal events, which could result in apparent diffusive argon loss. Compared to the zircon U–Pb ages, the younger biotite $^{40}\text{Ar}/^{39}\text{Ar}$ ages imply a possible thermal disturbance. However, the biotite $^{40}\text{Ar}*/^{39}\text{Ar}$ ratios are relatively consistent in each fractionation across different heating steps and yield similar apparent ages with a flat age spectrum [16]. The plateau ages have a close relationship with the isochron ages [16]. The observation thus precludes the possibility of a subsequent thermal disturbance. The biotite $^{40}\text{Ar}/^{39}\text{Ar}$ geochronology is sufficiently reliable to constrain the timing of cooling. The average biotite $^{40}\text{Ar}/^{39}\text{Ar}$ age is ~ 3 million years younger than that of alkali-feldspar granite, which corresponds to the estimated duration from magma emplacement to biotite Ar–Ar closure. We therefore hypothesize that the Tiantangshan tin polymetallic deposit experienced a prolonged magmatic-hydrothermal process that might have lasted for at least 3 million years.

Recent advances in the dating of tin deposits, such as the employment of zircon or cassiterite U–Pb, Molybdenite Re–Os and muscovite or biotite Ar–Ar isotopic ages, have enabled researchers to characterize the magmatic-hydrothermal process and cooling history of tin deposits with excellent precision. The biotite $^{40}\text{Ar}/^{39}\text{Ar}$ plateau age ($135.1 \pm 0.8\text{ Ma}$) is ~ 3 million years younger than the zircon U–Pb age of the biotite monzonitic granite porphyry in the Feie’shan W–Sn deposit ($139.2 \pm 1.7\text{ Ma}$) [35]. The muscovite $^{40}\text{Ar}/^{39}\text{Ar}$ plateau age ($140.6 \pm 1.0\text{ Ma}$) is ~ 4 million years younger than the cassiterite U–Pb age ($145.8 \pm 0.6\text{ Ma}$) in the Xiling tin deposit [36]. Two muscovite samples collected from greisen W–Mo–Be ores and W–Mo-bearing muscovite-quartz stockwork ores yield $^{40}\text{Ar}/^{39}\text{Ar}$ plateau ages of $146.85 \pm 0.8\text{ Ma}$ and $146.31 \pm 0.75\text{ Ma}$, respectively, which are both ~ 6 million years younger than that of the granite in the Xiatongling W–Mo–Be deposit ($154.7 \pm 1.7\text{ Ma}$) [37]. The Sn–Nb–Ta bearing Jinzhuyuan granite in limu mining district show a U–Pb age of $218.3 \pm 2.4\text{ Ma}$ with a muscovite $^{40}\text{Ar}/^{39}\text{Ar}$ plateau age of $212.4 \pm 1.4\text{ Ma}$ and isochron age of $213.2 \pm 2.2\text{ Ma}$ [38]. The magmatic crystallization, ore formation, and the related alteration all occurred over a short interval of less than 6 million years in the Taoxikeng tungsten deposit [39].

5.2. Genetic Type, Origin and Tectonic Background of the Tiantangshan A-Type Granite

Both the Tiantangshan alkali-feldspar granite and trachydacite exhibit a strong A-type affinity [10,34,40,41], as evidenced by their enrichment in REEs (except for Eu, Figure 6) and HFSEs ($\text{Zr} + \text{Nb} + \text{Ce} + \text{Y} > 350\text{ ppm}$), depletion in Ba and Sr (Figure 6), as well as high Ga/Al ratios (Figure 8a). The relatively low Yb/Ta and Y/Nb ratios further indicate that these granitic rocks should be classified as A₁ subtype (Figure 8b).

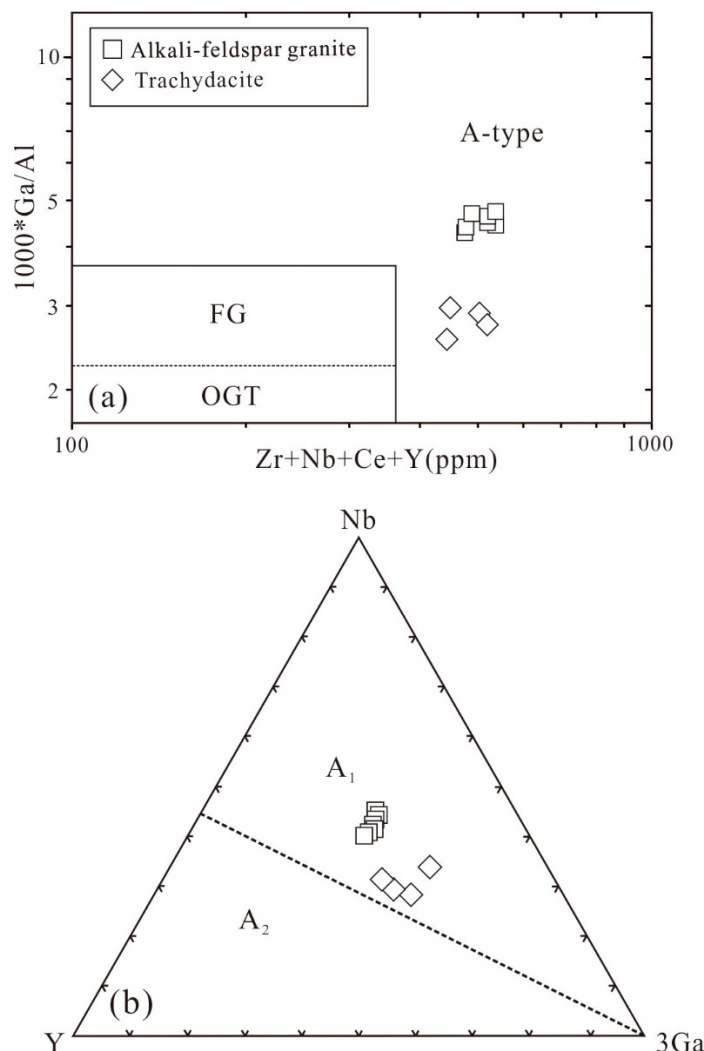


Figure 8. (a) $\text{Zr} + \text{Nb} + \text{Ce} + \text{Y}$ vs. $10000 * \text{Ga/Al}$ [34] and (b) representative triangular plots for distinguishing between A₁ and A₂ granitoids [9] for Tiantangshan alkali-feldspar granite.

A-type magmas were suggested to result from the partial melting of specific crustal protoliths [34,40,42] or from the extensive fractional crystallization from mantle-derived basaltic magmas [43]. The A₁ subtype generally share similar Nb/Ta and Y/Nb ratios as oceanic-island basalts, whereas their counterparts bear a geochemical resemblance to average crust and island-arc basalts [9] (Figure 8b). The Tiantangshan alkali-feldspar granite and trachydacite belong to the A₁ subtype and plot in the OIB field, presumably indicating that they were derived from an OIB-like source. Furthermore, the Nd isotopic compositions of these granite are similar to those of coeval (~140 Ma) OIB-like mafic rocks in northern Guangdong (−5.89 to 5.16), suggesting that they might have derived from the AFC of basaltic magmas (Figure 7). The fact that of the alkali-feldspar granite and OIB share similar Nb/Ta and Y/Nb ratios strongly implies that they may represent the mantle differentiates with less continental crust contamination in their origin. The evolved elemental ratios of the trachydacite suggest that they were contaminated with continental crust to a greater extent than the alkali-feldspar granite (Figure 9). This is further supported by the fact that the trachydacite exhibit high $\varepsilon_{\text{Nd}}(t)$ and negative Nb-Ta anomalies (Figure 7). Taken together, we conclude that the Tiantangshan A₁-type granite were generated from the AFC of the coeval OIB-like mafic magma. The A-type granite is hypothesized to have formed at extensional tectonic background [9,40]. The Late Mesozoic magmatism and mineralization of SE China are generally considered to be related to the subduction of the Palaeo-Pacific plate, for which a number of models have been proposed [20,44–46]. More recently, a new repeated slab-advance-retreat

model of the Palaeo-Pacific plate was developed based on geochronological and geochemical data of Late Triassic to Early Jurassic mafic rocks and Early Jurassic A-type granites in southern Jiangxi and western Fujian Provinces [15]. According to this repeated slab-advance-retreat model, the formation of the Early Cretaceous (141–124 Ma) A-type granite belt (Figure 1) was a result of the regional extension caused by the progressive slab rollback. Our new data presented in this paper lent further support to this model. The origin of the Early Cretaceous Tiantangshan A-type granite suggests the development of a back-arc extension along the Early Cretaceous A-type granite belt since the beginning of Early Cretaceous as a consequence of slab rollback [15]. Such an extension caused lithosphere thinning and the concomitant asthenosphere upwelling. The underplating of basaltic magma could trigger partial melting of the thinned lower-crust rocks, leading to the formation of the Early Cretaceous A₂ type granites. On the other hand, the AFC of the underplated basaltic magma could subsequently give rise to the Tiantangshan A₁ type granite. Therefore, the Tiantangshan tin polymetallic deposit might have generated in an extensional tectonic regime caused by slab rollback of the Paleo-Pacific Plate.

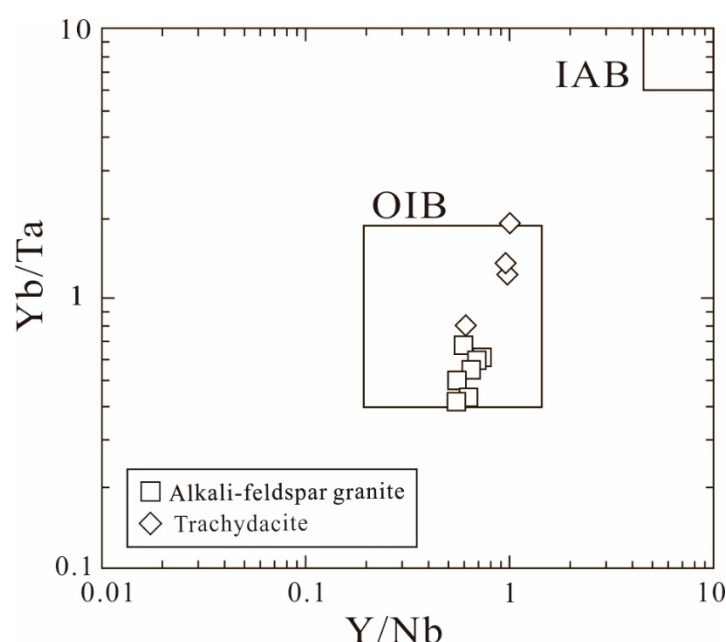


Figure 9. Y/Ta vs. Y/Nb diagrams for A-type granite [9].

5.3. A-Type Granite and Tin Mineralization

Magmatic differentiation plays a crucial role in the formation of tin bearing granite [3]. The in situ fractional crystallization of tin granitic rocks is characterized by a remarkable decrease in the level of Rb and depletion of Ba and Sr [2]. Consistent with this, the Tiantangshan alkali-feldspar granite generally exhibit low abundance of Sr and Ba, as well as increased levels of SiO₂, suggesting that they were derived from fractional crystallization. Continued fractional crystallization in the rest of the melts led to enrichment of Sn, W, Ta, Rb, Cs, F and Li, as well as depletion of Ti, U, Th, Ba, Sr, Zr. Among these elements, Ti and Ta are representative of distinct enrichment or depletion. TiO₂/Ta ratio is, thus, a good indicator of the evolution degree of granitic magma differentiation [4]. Moreover, Rb and Li may be affected by the hydrothermal processes, whereas Ta and Ti are relatively stable. The TiO₂/Ta ratios show a progressive decline from 4900 in the less differentiated granodiorite to <1 in the most differentiated granite from the Marche area [4]. In general, the TiO₂/Ta ratio of the Tiantangshan alkali-feldspar granite is inversely correlated to the level of Sn (Figure 10). In contrast with alkali-feldspar granite, trachydacite has a comparatively lower content of SiO₂, but elevated levels of Sr, Ba (Tables 2 and 3) and TiO₂/Ta ratio (Figure 10). All of these geochemical features imply that trachydacite experienced less differentiation than the alkali-feldspar granite. Furthermore, all

except one trachydacite sample (which might have been affected by greisenization at a later stage) that we analyzed contain less Sn than the alkali-feldspar granite (Tables 2 and 3). We, therefore, suggest that Sn enrichment of Tiantangshan tin deposit is more likely related to the Tiantangshan alkali-feldspar granite than the trachydacites. Another possible explanation is that these granitic rocks could have inherited their geochemical specialization from their source rocks during the partial melting. However, TiO_2 -Sn and Rb/Sr-Sn binary diagrams of the granitic fractionation series from various tin and non-tin provinces do not seem to support this hypothesis [1]. Previous studies showed that source rocks generally contribute a maximum of 5–10 ppm of Sn. Instead, the observed Sn enrichment is more likely to have resulted from the fractional crystallization of tin bearing granitic rocks. Both Tiantangshan alkali-feldspar granite and the trachydacite are derived from same source rock via AFC. The observation that the less differentiated trachydacite generally have lower Sn contents than the highly differentiated alkali-feldspar granite provides further support to this view.

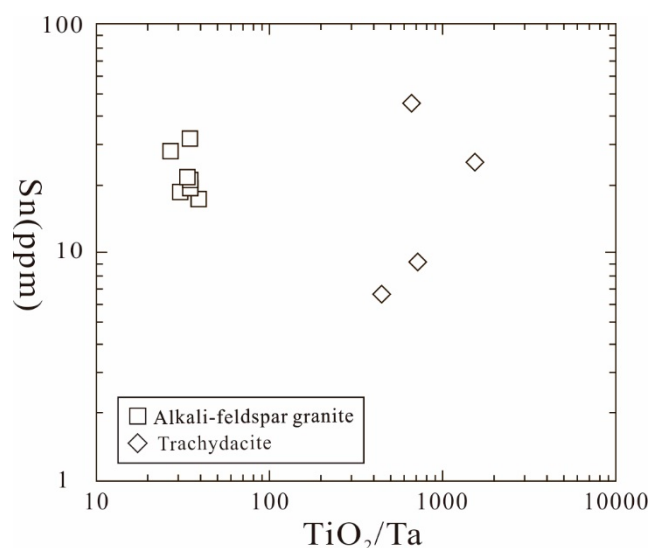


Figure 10. TiO_2/Ta vs. Sn diagrams of the Tiantangshan granitic rocks.

Prolonged fractional crystallization leads to concentration of H_2O and other volatiles in the rest liquid. Free water could react with the granite causing it to be gradually converted into greisen. The beginning of greisenization is characterized by the alteration of K-feldspar into muscovite (Figure 4d), which is illustrated by the following reaction: $3\text{KAlSi}_3\text{O}_8 + 2\text{H}^+ = \text{KAl}_3\text{Si}_3\text{O}_{10}(\text{OH})_2 + 6\text{SiO}_2 + 2\text{K}^+$. Sn is generally considered to exist as Sn^{2+} or Sn^{4+} in complexation with Cl^- in the fluid [47]. Lowering the HCl activity in the fluid system leads to the precipitation of the cassiterite as manifested by $(\text{SnCl}_4[\text{H}_2\text{O}]_2)^0 = \text{SnO}_2 + 4\text{HCl}$ and $(\text{SnCl}_3)^- + \text{H}^+ + 2\text{H}_2\text{O} = \text{SnO}_2 + 3\text{HCl} + \text{H}_2$. Greisenization is, therefore, a good catalytic reaction for the precipitation of cassiterite. The magmatic-hydrothermal process lasted at least ~3 million years and produced at least one hydrothermal pulse, which resulted in the generation of the hydrothermal biotite at ~133 Ma.

6. Conclusions

1. The SHRIMP zircon U-Pb dating of the alkali-feldspar granite and the trachydacite in the Tiantangshan tin polymetallic deposit yields $^{206}\text{Pb}/^{238}\text{U}$ ages of 138.4 ± 1.2 and 136.2 ± 1.2 Ma, respectively. The Tiantangshan tin polymetallic deposit experienced a prolonged magmatic-hydrothermal process over a period of ~3 million years from the emplacement of granitic rocks to the origination of the hydrothermal biotite.
2. Both the Tiantangshan alkali-feldspar granite and trachydacite can be classified as A₁-type granite based on geochemical evidence. These granitic rocks were derived from the AFC of the coeval

OIB-like basaltic magma in an extensional setting, which was most likely caused by the rollback of the Paleo-pacific plate.

3. The tin polymetallic mineralization is associated with the Tiantangshan A₁ type alkali-feldspar granite.

Author Contributions: R.-Y.J., L.G., Z.-S.P., H.-X.J., Z.-H.Z., H.C., G.-C.W., Z.L. did the field work; R.-Y.J., G.-C.W., Z.L. analyzed results of all the experiments; R.-Y.J., G.-C.W. wrote the paper; R.-Y.J., G.-C.W., L.G., Z.-S.P., Z.L. revised the manuscript. All authors read and approved the manuscript.

Funding: This study was financially supported by National Key Research and Development Program of China (Grant 2017YFC0601506), Geological Survey Project of China Geological Survey (Grant DD20190570) National Natural Science Foundation of China (Grant 41703022), Fundamental Research Funds for the Central Universities (Izujbky-2018-52), Plateau mountain ecology and earth's environment discipline construction project (Grant C176240107), Joint Foundation Project between Yunnan Science and Technology Department and Yunnan University (Grant C176240210019), Geology Discipline Construction Project of Yunnan University (C176210227), Science (Engineering) Research Project of Yunnan University(2017YDQN08).

Acknowledgments: We thank the senior engineers Hongren Chen and other local geologists from the Bureau of Geology for Nuclear Industry of Guangdong Province for their assistance in the field.

Conflicts of Interest: The authors declare no conflict of interest.

References

1. Lehmann, B. Metallogeny of tin; magmatic differentiation versus geochemical heritage. *Econ. Geol.* **1982**, *77*, 50–59. [[CrossRef](#)]
2. Groves, D.I.; McCarthy, T.S. Fractional crystallization and the origin of tin deposits in granitoids. *Miner. Depos.* **1978**, *13*, 11–26. [[CrossRef](#)]
3. Lehmann, B. Tin granites, geochemical heritage, magmatic differentiation. *Geol. Rundsch* **1987**, *76*, 177–185. [[CrossRef](#)]
4. Boissavy-Vinau, M.; Roger, G. The TiO₂/Ta ratio as an indicator of the degree of differentiation of tin granites. *Miner. Depos.* **1980**, *15*, 231–236. [[CrossRef](#)]
5. Liverton, T.; Botelho, N.F. Fractionated alkaline rare-metal granites: Two examples. *J. Asian Earth Sci.* **2001**, *19*, 399–412. [[CrossRef](#)]
6. Haapala, I.; Lukkari, S. Petrological and geochemical evolution of the Kymi stock, a topaze granite cupola within the Wiborg rapakivi batholith, Finland. *Lithos* **2005**, *80*, 247–362. [[CrossRef](#)]
7. Chen, J.; Wang, R.C.; Zhu, J.C.; Lu, J.J.; Ma, D.S. Multiple-aged granitoids and related tungsten-tin mineralization in the Nanling Range: South China. *Sci. China Earth Sci.* **2013**, *56*, 2045–2055. [[CrossRef](#)]
8. Loiselle, M.C.; Wones, D.R. Characteristics and origin of anorogenic granites. *Geol. Soc. Am. Abstr. Programs* **1979**, *11*, 468.
9. Eby, G.N. Chemical subdivision of the A-type granitoids: Petrogenetic and tectonic implications. *Geology* **1992**, *20*, 641–644. [[CrossRef](#)]
10. Eby, G.N. The A-type granitoids: A review of their occurrence and chemical characteristics and speculations on their petrogenesis. *Lithos* **1990**, *26*, 115–134. [[CrossRef](#)]
11. Mao, J.W.; Cheng, Y.B.; Chen, M.H.; Pirajno, F. Major types and time-space distribution of Mesozoic ore deposits in South China and their geodynamic settings. *Miner. Depos.* **2013**, *48*, 267–294. [[CrossRef](#)]
12. Chen, J.; Lu, J.J.; Chen, W.F.; Wang, R.C.; Ma, D.S.; Zhu, J.C.; Zhang, W.L.; Ji, J.F. W-Sn-Nb-Ta-bearing granites in the Nanling Range and their relationship to metallogensis. *Geol. J. China Univ.* **2008**, *14*, 459–473. (in Chinese with English abstract).
13. Zhou, Y.; Liang, X.Q.; Liang, X.R.; Wu, S.C.; Jiang, Y.; Wen, S.N.; Cai, Y.F. Geochronology and geochemical characteristics of the Xitian tungsten-tin-bearing A-type granite, Hunan Province, China. *Geotecton. Metallog.* **2013**, *37*, 517–535. (in Chinese with English abstract).
14. Zheng, W.; Mao, J.W.; Zhao, H.J.; Zhao, C.S.; Yu, X.F. Two Late Cretaceous A-type granites related to the Yingwuling W-Sn polymetallic mineralization in Guangdong province, South China: Implications for petrogenesis, geodynamic setting, and mineralization. *Lithos* **2017**, *274*, 106–122. [[CrossRef](#)]
15. Jiang, Y.H.; Wang, G.C.; Liu, Z.; Ni, C.Y.; Qing, L.; Zhang, Q. Repeated slab-advance retreat of the Palaeo-Pacific plate underneath SE China. *Int. Geol. Rev.* **2015**, *57*, 472–491. [[CrossRef](#)]

16. Jia, H.X.; Pang, Z.S.; Chen, R.Y.; Xue, J.L.; Chen, H.; Lin, L.J. Genesis and hydrothermal evolution of the Tiantangshan tin-polymetallic deposit, south-eastern Nanling Range, South China. *Geol. J.* **2018**, *1–22*. [[CrossRef](#)]
17. Carter, A.; Roques, D.; Bristow, C.; Kinny, P. Understanding Mesozoic accretion in Southeast Asia: Significance of Triassic thermotectonism (Indosinian orogeny) in Vietnam. *Geology* **2001**, *29*, 211–214. [[CrossRef](#)]
18. Lepvrier, C.; Maluski, H.; Tich, V.; Leyreloup, A.; Truong Thi, P.; Van Vuong, N. The Early Triassic Indosinian orogeny in Vietnam (Truong Son Belt and Kontum Massif); implications for the geodynamic evolution of Indochina. *Tectonophysics* **2004**, *393*, 87–118. [[CrossRef](#)]
19. Ernst, W.G.; Tsujimori, T.; Zhang, R.; Liou, J.G. Permo-Triassic collision, subduction zone metamorphism, and tectonic exhumation along the East Asian continental margin. *Ann. Rev. Earth Planet. Sci.* **2007**, *35*, 73–110. [[CrossRef](#)]
20. Zhou, X.M.; Sun, T.; Shen, W.Z.; Shu, L.S.; Niu, Y.L. Petrogenesis of Mesozoic granitoids and volcanic rocks in South China: A response to tectonic evolution. *Episodes* **2006**, *29*, 21–26.
21. Zhou, X.M.; Li, W.X. Origin of late Mesozoic igneous rocks in southeastern China: Implications for lithosphere subduction and underplating of mafic magmas. *Tectonophysics* **2000**, *326*, 269–287. [[CrossRef](#)]
22. Mao, J.W.; Xie, G.Q.; Guo, C.L.; Yuan, S.D.; Cheng, Y.B.; Chen, Y.C. Spatial-temporal distribution of Mesozoic ore deposits in South China and their metallogenic settings. *Geol. J. China Univ.* **2008**, *14*, 510–526, (in Chinese with English abstract).
23. Williams, I.S. U-Th-Pb geochronology by ion microprobe. *Rev. Econ. Geol.* **1998**, *7*, 1–35.
24. Ballard, J.R.; Palin, J.M.; Williams, I.S.; Campbell, I.H.; Faunes, A. Two ages of porphyry intrusion resolved for the super-giant Chuquicamata copper deposit of northern Chile by ELA-ICP-MS and SHRIMP. *Geology* **2001**, *29*, 383–386. [[CrossRef](#)]
25. Nasdala, L.; Hofmeister, W.; Norberg, N.; Martinson, J.M.; Corfu, F.; Dörr, W.; Kamo, S.L.; Kennedy, A.K.; Kronz, A.; Reiners, P.W.; et al. Zircon M257-a homogeneous natural reference material for the ion microprobe U–Pb analysis of zircon. *Geostand Geoanal Res.* **2008**, *32*, 247–265. [[CrossRef](#)]
26. Black, L.P.; Kamo, S.L.; Allen, C.M.; Aleinikoff, J.N.; Davis, D.W.; Korsch, R.J.; Foudoulis, C. TEMORA 1: A new zircon standard for Phanerozoic U–Pb geochronology. *Chem. Geol.* **2003**, *200*, 155–170. [[CrossRef](#)]
27. Ludwig, K.R. *Squid 1.02: A User's Manual*; Berkeley Geochronology Centre Special Publication: Berkeley, CA, USA, 2001; pp. 1–19.
28. Gao, J.F.; Lu, J.J.; Lai, M.Y.; Lin, Y.P.; Pu, W. Analysis of trace elements in rock samples using HR-ICPMS (Natural Sciences). *J. Nanjing Univ.* **2003**, *39*, 844–850.
29. Pu, W.; Zhao, K.D.; Ling, H.F.; Jiang, S.Y. High precision Nd isotope measurement by Triton TI Mass Spectrometry. *Acta Geosci. Sin.* **2004**, *25*, 271–274, (in Chinese with English abstract).
30. Pu, W.; Gao, J.F.; Zhao, K.D.; Ling, H.F.; Jiang, S.Y. Separation method of Rb–Sr, Sm–Nd using DCTA and HIBA (Natural Sciences). *J. Nanjing Univ.* **2005**, *41*, 445–450.
31. Boynton, W.V. Cosmochemistry of the rare earth elements: Meteorite studies. In *Rare Earth Element Geochemistry*; Henderson, P., Ed.; Elsevier: Amsterdam, The Netherlands, 1984; pp. 63–114. [[CrossRef](#)]
32. McDonough, W.F.; Sun, S.S. Isotopic and geochemical systematics in Tertiary–Recent basalts from southeastern Australia and implication for the sub-continental lithosphere. *Geochim. Cosmochim. Acta* **1985**, *49*, 2051–2067. [[CrossRef](#)]
33. Li, X.H.; McCulloch, M.T. Geochemical characteristics of Cretaceous mafic dikes from northern Guangdong, SE China: Age, origin and tectonic significance. Mantle Dynamics and Plate Interactions in East Asia. *AGU Geodyn. Ser.* **1998**, *27*, 405–419.
34. Whalen, J.B.; Currie, K.L.; Chappell, B.W. A-type granites: Geochemical characteristics, discrimination and petrogenesis. *Contrib. Mineral. Petrol.* **1987**, *95*, 407–419. [[CrossRef](#)]
35. Liu, P.; Mao, J.W.; Cheng, Y.B.; Yao, W.; Wang, X.Y.; Hao, D. An Early Cretaceous W-Sn deposit and its implications in southeast coastal metallogenic belt: Constraints from U–Pb, Re-Os, Ar-Ar geochronology at the Feie'shan W-Sn deposit, SE China. *Ore Geol. Rev.* **2017**, *81*, 112–122. [[CrossRef](#)]
36. Liu, P.; Mao, J.W.; Santosh, M.; Xu, L.G.; Zhang, R.Q.; Jia, L.H. The Xiling Sn deposit, Eastern Guangdong Province, Southeast China: A new genetic model from $^{40}\text{Ar}/^{39}\text{Ar}$ muscovite and U–Pb cassiterite and zircon geochronology. *Econ. Geol.* **2018**, *113*, 511–530. [[CrossRef](#)]
37. Li, X.F.; Yi, X.K.; Huang, C.; Wang, C.Z.; Wei, X.L.; Zhu, Y.T.; Xu, J. Zircon U–Pb, molybdenite Re-Os and muscovite Ar-Ar geochronology of the Yashan W-Mo and Xiatongling W-Mo-Be deposits: Insights for the

- duration and cooling history of magmatism and mineralization in the Wugongshan district, Jiangxi, South China. *Ore Geol. Rev.* **2018**, *102*, 1–17. [CrossRef]
38. Feng, Z.; Kang, Z.; Yang, F.; Liao, J.; Wang, C. Geochronology of the Limu W–Sn–Nb–Ta-Bearing Granite Pluton in South China. *Resour. Geol.* **2013**, *63*, 320–329. [CrossRef]
39. Guo, C.; Mao, J.; Bierlein, F.; Chen, Z.; Chen, Y.; Li, C.; Zeng, Z. SHRIMP U–Pb (zircon), Ar–Ar (muscovite) and Re–Os (molybdenite) isotopic dating of the Taoxikeng tungsten deposit, South China Block. *Ore Geol. Rev.* **2011**, *43*, 26–39. [CrossRef]
40. Collins, W.J.; Beams, S.D.; White, A.J.R. Nature and origin of A-type granites with particular reference to southeastern Australia. *Contrib. Mineral. Petrol.* **1982**, *80*, 189–200. [CrossRef]
41. Jiang, Y.H.; Jiang, S.Y.; Ling, H.F.; Zhou, X.R.; Rui, X.J.; Yang, W.Z. Petrology and geochemistry of shoshonitic plutons from the western Kunlun orogenic belt, northwestern Xinjiang, China: Implications for granitoid geneeses. *Lithos* **2002**, *63*, 165–187. [CrossRef]
42. Creaser, R.A.; Price, R.C.; Wormald, R.J. A-type granites revisited: Assessment of a residual source model. *Geology* **1991**, *19*, 163–166. [CrossRef]
43. Turner, S.P.; Foden, J.D.; Morrison, R.S. Derivation of some A-type magmas by fractionation of basaltic magma: An example from the Padthaway Ridge, South Australia. *Lithos* **1992**, *28*, 151–179. [CrossRef]
44. Lapierre, H.; Jahn, B.M.; Charvet, J. Mesozoic felsic arc magmatism and continental olivine tholeiites in Zhejiang province and their relationship with the tectonic activity in southeastern China. *Tectonophys* **1997**, *274*, 321–338. [CrossRef]
45. Jiang, Y.H.; Jiang, S.Y.; Dai, B.Z.; Liao, S.Y.; Zhao, K.D.; Ling, H.F. Middle to Late Jurassic felsic and mafic magmatism in southern Hunan Province, Southeast China: Implications for a continental arc to rifting. *Lithos* **2009**, *107*, 185–204. [CrossRef]
46. Li, Z.X.; Li, X.H. Formation of the 1300-km-wide intracontinental orogen and postorogenic magmatic province in Mesozoic South China: A flat-slab subduction model. *Geology* **2007**, *35*, 179–182. [CrossRef]
47. Wilson, G.A. Cassiterite solubility and Metal Chloride Speciation in Supercritical Solutions. Ph.D. Thesis, John Hopkins University, Baltimore, MD, USA, 1986.



© 2019 by the authors. Licensee MDPI, Basel, Switzerland. This article is an open access article distributed under the terms and conditions of the Creative Commons Attribution (CC BY) license (<http://creativecommons.org/licenses/by/4.0/>).